

This is the author's final, peer-reviewed manuscript as accepted for publication. The publisher-formatted version may be available through the publisher's web site or your institution's library.

MoS₂/Graphene Composite Paper for Sodium-Ion Battery Electrodes

Lamuel David, Romil Bhandavat, and Gurpreet Singh

How to cite this manuscript

If you make reference to this version of the manuscript, use the following information:

David, L., Bhandavat, R., & Singh, G. (2014). MoS₂/graphene composite paper for sodium-ion battery electrodes. Retrieved from <http://krex.ksu.edu>

Published Version Information

Citation: David, L., Bhandavat, R., & Singh, G. (2014). MoS₂/graphene composite paper for sodium-ion battery electrodes. *ACS Nano*, 8(2), 1759-1770.

Copyright: © 2014 American Chemical Society

Digital Object Identifier (DOI): 10.1021/nn406156b

Publisher's Link: <http://pubs.acs.org/doi/abs/10.1021/nn406156b>

This item was retrieved from the K-State Research Exchange (K-REx), the institutional repository of Kansas State University. K-REx is available at <http://krex.ksu.edu>

MoS₂/graphene Composite Paper For Sodium-Ion Battery Electrodes

Lamuel David, Romil Bhandavat and Gurpreet Singh*

*Mechanical and Nuclear Engineering Department, Kansas State University,
Manhattan, Kansas, 66506, United States*

**E-mail: gurpreet@ksu.EDU. Tel.: +1-785-532-7085. Fax: +1-785-532-7057*

ABSTRACT

We study the synthesis, electrochemical and mechanical performance of layered freestanding papers composed of acid exfoliated few layer molybdenum disulfide (MoS₂) and reduced graphene oxide (rGO) flakes for use as a self-standing flexible electrode in sodium ion batteries. Synthesis was achieved through vacuum filtration of homogenous dispersions consisting of varying wt. % of acid treated MoS₂ flakes in GO in DI water, followed by thermal reduction at elevated temperatures. The electrochemical performance of the crumpled composite paper (at 4 mg.cm⁻²) was evaluated as counter electrode against pure Na foil in a half-cell configuration. The electrode showed good Na cycling ability with a stable charge capacity of approx. 230 mAh.g⁻¹ with respect to total weight of the electrode with coulombic efficiency reaching approx. 99 %. In addition, static uniaxial tensile tests performed on crumpled composite papers showed high average strain to failure reaching approx. 2 %.

KEYWORDS: TMDC, sodium battery, freestanding electrode, graphene, MoS₂

Lithium ion batteries (LIBs) have been extensively studied for energy-storage applications like portable electronic devices and electric vehicles.¹⁻³ However, concerns over the cost, safety and availability of Li reserves⁴ for large-scale applications involving renewable energy integration and the electrical grid have to be answered. In this regard, sodium ion batteries (SIBs) have drawn increasing attention because in contrast to lithium,⁵⁻⁷ sodium resources are practically inexhaustible and evenly distributed around the world while the ion insertion chemistry is largely identical to that of lithium. Also, from electrochemical point of view, sodium has a very negative redox potential (-2.71 V, vs. SHE) and a small electrochemical equivalent (0.86 gAh⁻¹), which make it the most advantageous element for battery applications after lithium. However, many challenges remain before SIBs can become commercially competitive with LIBs. For instance, Na ions are about 55% larger in radius than Li-ions, which makes it difficult to find a suitable host material to allow reversible and rapid ion insertion and extraction.⁸

To this end, researchers have proposed a number of high-capacity sodium host materials (negative electrode) involving either carbon or group IVA and VA elements that form intermetallic compounds with Na.⁹⁻¹³ The alloying compounds demonstrate high first cycle Na-storage capacities, such as Na₁₅Sn₄ (847 mAhg⁻¹), Na₁₅Pb₄ (485 mAhg⁻¹), Na₃Sb (600 mAhg⁻¹) and Na₃P (2560 mAhg⁻¹), respectively. However, this comes at the cost of very high volume change upon Na-insertion (as much as 500 % in some cases), resulting in formation of internal cracks, loss of electrical contact, and eventual failure of the electrode (particularly for thick electrodes).¹⁴ Novel nanostructured designs that can accommodate large volumetric strains need further exploration.¹⁵⁻¹⁸ For carbon-based electrode materials, much of the emphasis has been on hard carbons due to large interlayer spacing and disordered structure.¹⁹⁻²⁵ For example, hard carbon prepared from pyrolyzed glucose, carbon black, and carbon microspheres have been shown to exhibit initial reversible capacities of 300 mAhg⁻¹, 200 mAhg⁻¹, and 285 mAhg⁻¹, respectively in a Na-ion cell.¹⁵⁻¹⁷ More recently, another hard carbon material that could deliver a reversible capacity of more than 200 mAhg⁻¹ over 100 cycles has been reported.^{22,25} However, these studies were conducted on traditional anode architecture (prepared through slurry coating of active material on metallic current collector foil and the

capacities reported were with respect to the active material only), either at low cycling current rates or at elevated temperatures. Overall, new electrode design and concepts based on chemistry other than alloying and ion intercalation must also be explored to realize improved performance in Na-ion batteries under normal operating conditions.

Studies on Li-ion batteries have shown that 2-D layered nanomaterials such as graphene and transition metal dichalcogenides (TMDCs such MoS₂, WS₂) are promising materials for efficient storage and release of Li-ions.²⁶⁻³⁷ However, when compared with graphite, the electrochemical lithiation in layered TMDCs is distinct as majority of the lithium is stored by means of a conversion reaction in which Li-ion reacts with the TMDC forming Li₂S and transition metal phases as the reaction products. More important, this type of a conversion reaction can allow transfer of 2 to 6 electrons per transition metal compared to single electron in the case of intercalation reaction (lithium/carbon system).^{1, 34} Although layered graphite has been ruled out for sodium-based systems (as Na ions do not tend to form staged intercalation compounds with graphite),³⁸⁻⁴⁰ a graphene based free-standing paper based electrode can provide a porous and flexible support structure for a TMDC to undergo a reversible conversion type reaction with Na-ions. It can also act an efficient electronic current collector, thereby eliminating the need for metallic substrate (generally a 10 μm thick foil at 10 mg.cm⁻²),^{41, 42} electrically conducting additives and polymeric binders that amount to a total of approx. 10 % of the cell weight⁴² in traditional negative electrodes.⁴³⁻⁴⁸ Herein, we provide the first report of (a) synthesis of composite papers from acid functionalized MoS₂ and reduced graphene oxide flakes, (b) improved capacity and high efficiency reversible Na storage in the self-standing flexible MoS₂/graphene electrodes at room temperatures, and (c) mechanical characterization that highlight the high strain to failure in these composite papers.

Results and Discussions

Layered “as-obtained” MoS₂ was exfoliated by mechanical sonication in chlorosulfonic acid followed by quenching in DI water (see methods section). A

digital image of the acid treated MoS₂ dispersion immediately after quenching in DI water is shown in Fig. 1a. From SEM observations, the particle size for MoS₂-raw was observed to be approx. 20 to 40 μm (Fig. 1b) while that of MoS₂-SA was less than 20 μm (Fig. 1c). Shown in Fig. 1(d-f) are high-magnification TEM images of acid-treated MoS₂ sheets. All the sheets were observed to be only a few layers thick with flake size ranging from 100 nm to 1 μm. From literature, we can correlate the reason for exfoliation of MoS₂ to electrostatic repulsion forces caused by protonation of MoS₂ surfaces.⁵⁰ Using DLVO theory, ζ potential measurements can quantify this surface charge on MoS₂ sheet and hence help in establishing the dispersion stability. For ζ potential measurements, the pH was varied by adding 0.01 M NaOH solution and since the contribution from dissociated OH⁻ ions in the measured potential is minimal, it was neglected in the analysis. The lower pH range was limited to protect the instrument electrode. The surface potential showed a range varying from -35 mV at pH of 4 to -60 mV at pH of 10, shown as an insert in Fig. 1g. As higher surface potential (negative) implies more stable suspensions, based on the obtained results, higher pH suggests a larger exposed MoS₂ sheet surface. This dependence of surface potential on pH is similar to that observed for exfoliated (surface-functionalized) graphene sheets by Coleman's group.⁵¹ Further, we used their model for graphene stabilization mechanism for explaining the superacid-MoS₂ interaction mechanism (see Supporting Information).^{51, 52} Fig. 1g is the plot for total interaction energy per unit area of the sheet (V_T/A).

Further analysis involved Raman spectroscopy and X-ray diffraction before and after acid treatment. Raman spectrum (Fig. 1h) obtained by use of 633 nm wavelength laser showed typical E¹_{2g}, A_{1g}, 2LA(M) and A_{1g}+LA(M) peaks at 380, 407, 460 and 641 cm⁻¹, respectively. The in-plane E¹_{2g} peak results from opposite vibration of two S atoms with respect to the Mo atom while the A_{1g} peak is associated with the out-of-plane vibration of only S atoms in opposite directions.^{53, 54} The intensity of A_{1g} peak arises from the resonance Raman (RR) scattering, because the incident laser is in resonance with the direct bandgap (~1.96 eV) at the K point. The asymmetric 2LA(M) peak is associated with second-order zone-edge phonon (LA(M)) and a first order optical phonon peak (A_{2u}).⁵⁵⁻⁵⁸ These results along with electron microscopy results suggests that the structure is relatively

undistorted MoS₂.⁵⁹⁻⁶⁰ Further, X-ray diffraction analysis (XRD) of MoS₂-raw and MoS₂-SA in Fig. 1i showed distinct peak at 14.3 ° and 13.97 ° 2θ, respectively. These peaks are associated with 002 reflection from the basal plane of MoS₂ with measured 'd' spacing of 3.1 Å and 3.2 Å lattice plane of hexagonal MoS₂ (JCPDS #37-1492). This suggests restacking of the MoS₂ layers upon drying.^{61, 62}

Later, the MoS₂/rGO papers were prepared by vacuum filtration of graphene oxide (GO) and molybdenum disulfide (MoS₂) sheets dispersed in water:isopropanol (1:1) solution, which is shown with the help of a schematic in Fig. 2a, while Fig. 2b is the digital image of one such paper synthesized using this technique. SEM images in Fig. 2c,d and Supplementary Fig. S1 (a through h) show the top-view and corresponding cross-section view of 60MoS₂, rGO, 20MoS₂, 40MoS₂ and 60MoS₂-raw free-standing papers, respectively. The papers were approx. 10 to 20 μm in thickness (that varied with the weight percentage of MoS₂ in GO) with a relatively homogeneous composition (Supplementary Fig. S2 for high-resolution image). The interleaved structure observed in the cross-sectional images is preferred for easy storage and release of larger Na-ions, particularly at higher current densities or C-rates. The digital photograph in insert of Supplementary Fig. S1 (a through d) confirms the outstanding structural flexibility of rGO and MoS₂/graphene specimens. Further analysis involved SEM-X-ray energy dispersive spectroscopy (EDX), shown in insert in Fig. 2c. The EDX spectra from spot 1(square) showed peaks at 0.27 KeV and 0.52 KeV, which correspond to carbon (85.43 at %) and oxygen (10.41 at %) Kα energy, respectively. The low oxygen content indicate that rGO was highly reduced and pristine. In addition to carbon and oxygen, two small peaks at 2.29 KeV and 2.3 KeV corresponding to molybdenum Lα (1.39 at. %) and sulfur Kα (2.78 at. %) energy, respectively were also observed. At spot 2, peaks corresponding to Mo (26.13 at. %) and S (46.48 at. %) were prominent when compared to that of carbon (24.39 at. %), which unambiguously confirm the presence of MoS₂ sheets in the composite. TEM images are shown in Fig. 2e and Supplementary Fig. S1 (i through l). It is clear that the rGO sheets were layered with few layers of MoS₂ forming a very good electron conductive layer and also a support structure for free-standing paper. The insert in Fig. 2e is the selected area electron diffraction (SAED) pattern that indicates multiple spot pattern, one of which is due to the

polycrystallinity of restacked rGO sheets while second set of spot pattern were due to MoS₂ sheets. The hexagonal spot pattern (insert of Supplementary Fig. S1i) indicate that the graphitic AB stacking was preserved in the lattice after thermal reduction. To further observe the distribution of MoS₂ in the composite, EDX elemental mapping was performed on the cross-section of 60MoS₂ specimen (Supplementary Fig. S3). A slightly higher percentage of elemental carbon (graphene) was observed on one end of the paper, which is somewhat typical in a high inclusion content (in this case MoS₂ in graphene) matrix.⁶³ Supplementary Table S1 summarizes the percentage of each element detected in the corresponding EDX map. Further evidence showing presence of MoS₂ in rGO was achieved through X-ray photoelectron spectroscopy (XPS) (Supplementary Fig. S4) that compares powered MoS₂-SA with 60MoS₂ paper before and after reduction. MoS₂ peaks that were present in the starting material were also present in the free-standing paper. Notable change was observed in the intensity of oxygen (O1s) and carbon (C1s) peaks for 60MoS₂ specimen (before and after reduction) due to addition of GO. Raman spectroscopy of 60MoS₂ paper (Supplementary Fig. S5) showed typical MoS₂ peaks at 373 (E_{2g}¹), 400 (A_{1g}), and 445 (2LA(M)) cm⁻¹ along with characteristic rGO D and G peaks at 1330 (D) and 1560 (G) cm⁻¹, respectively. X-ray analysis (Supplementary Fig. S6) of 60MoS₂ paper also confirmed presence of rGO (JCPDS #01-0646) and MoS₂ (JCPDS #37-1492) in the composite. Further, the exact amount of MoS₂ in the final composite paper (after reduction) was inferred by carrying out thermogravimetric analysis (TGA) in flowing air. As can be seen in Fig. 2f, rGO and MoS₂ had oxidation events at approx. 450 and 700 °C, respectively. From the TGA data it was observed that thermally reduced 60MoS₂, 40MoS₂ and 20MoS₂ papers had approx. 73, 53 and 35 wt. % of MoS₂ in rGO.

Later, the effect of change in filler concentration on electrical conductivity of the composite was studied by use of a four-point measurement technique, which is presented in Fig. 2g. The increase in conductivity with increasing rGO concentration in the composite was somewhat not linear. This type of behavior is typical when electrically insulating filler (MoS₂) is added to a relatively conducting matrix (rGO) because significant increase in conductivity can only occur after the first conducting path through the sample is formed.⁶⁴⁻⁶⁵

Electrochemical performance

Supplementary Fig. S7 depict the voltage charge/discharge and differential capacity curves for various paper electrodes with varying MoS₂ content. Supplementary Fig. S7a shows the voltage profiles of rGO for 1st and 2nd cycle. The first cycle discharge and charge capacities were 784 mAhg⁻¹ and 86 mAhg⁻¹. The differential capacity profiles in Supplementary Fig. S7b showed a primary reduction peak at 200 mV, a secondary reduction peak at 610 mV and a weak oxidation peak at 0.9 V. The peak at 200 mV, which is present in all subsequent cycles, is associated with intercalation of rGO, while the peak at 610 mV suggests formation of solid electrolyte interphase (SEI) layer, which exists only in the first cycle. Supplementary Fig. S7 c, d shows the initial charge/discharge voltage profile and differential capacity curves for 20MoS₂ electrode. In the first cycle there are three reduction peaks. Peak at 150 mV that is attributed to MoS₂ /rGO intercalation while those at 580 mV and 0.8 V are attributed to SEI formation in rGO and MoS₂, respectively as these were present only during the first cycle. Only one subtle anodic peak at 1.35 V was observed. As the percentage of MoS₂ increased from 40 % (Supplementary Fig. S7e, f) and 60 % (Fig. 3 a, b), the domination of Na intercalation in MoS₂ over rGO increased which was evidently seen with increase in the intensity of the reduction peak at around 0.8 V and 0.9 V in the first cycle (peak at 580 mV observed in rGO electrode was relatively absent). In the case of 60MoS₂-raw (Supplementary Fig. S7 g,h) electrode, similar peaks to that of 60MoS₂ were observed.

Later, reaction kinetics of rGO and 60MoS₂ electrodes were compared by performing Galvanostatic intermittent titration (GITT) cycling and calculating the reaction resistance to Na insertion and extraction for the two electrodes. For rGO electrode (Supplementary Fig. S8 a, c, e), the reaction resistance for Na insertion was observed to be fairly constant at ~10 Ohm.g (or less) while it increased exponentially to ~50 Ohm.g in case of Na extraction at an extraction voltage of ~ 1.25 V. For MoS₂ electrode (Supplementary Fig. S8 b, d, f), reaction resistance increased gradually to ~20 Ohm.g during Na insertion. However, for the extraction half, the resistance remained stable at ~20 Ohm.g until approx. 2.5 V and then saw

a sudden increase reaching ~ 50 Ohm.g. The sudden increase in reaction resistance could be attributed to successive stage transformation processes during sodiation/desodiation or lithiation/delithiation observed in layered intercalation compounds.⁶⁶ Interestingly, both the electrodes showed a reaction resistance value of ~ 10 Ohm.g during initial insertion (discharge) in the upper voltage range of 2 to 1.0 V (Supplementary Fig. S8 c, d). This suggests that the initial Na insertion in 60MoS₂ composite electrode in the upper voltage range could be an intercalation reaction, which is later, followed by a conversion type reaction in the lower voltage range (indicated by rise in resistance).

Fig. 3c shows the charge capacities and columbic efficiency of rGO, 20MoS₂, 40MoS₂, 60MoS₂ and 60MoS₂-raw anodes cycled at a constant current density of 25 mA g⁻¹. For rGO, the charge capacity was stable at ~ 70.5 mAhg⁻¹ in the 20th cycle, while the high irreversible first cycle capacity is attributed to electrochemical reaction contributing to SEI layer formation. In the case of rGO/ MoS₂ composite electrodes, the first cycle charge capacity increased with increasing percentage of MoS₂ in the composite *i.e.*, 20MoS₂, 40MoS₂, and 60MoS₂ showed 139 mAhg⁻¹, 263 mAhg⁻¹, and 338 mAhg⁻¹, respectively. After initial drop in the capacity, rGO/ MoS₂ composite electrode remained constant at 123, 172 and 218 mAhg⁻¹ for 20MoS₂, 40MoS₂ and 60MoS₂, respectively. 60MoS₂ anode was the best performing with 83 % capacity retention and approx. 98 % average efficiency. While MoS₂-raw electrode showed a first cycle charge capacity of 233 mAhg⁻¹ that reduced to below ~ 100 mAhg⁻¹ after 20 cycles. For MoS₂-raw electrode, it is possible that the formation of SEI with successive cycles (and un-exfoliated nature of the flakes), may have hindered the diffusion of Na into the bulk of the specimen, resulting in capacity fading on consecutive cycling. While for acid treated MoS₂-SA electrode the more open and interleaved structure enabled it to utilize the entire bulk of the material in the electrode resulting in exceptional cyclic stability. Presence of conducting graphene sheets further provided the necessary platform on which volume or morphology changes due to conversion reaction could occur without any breakdown in the electrical contact.

Later, the composite paper electrode with maximum possible MoS₂ loading (*i.e.*, 90 % MoS₂ in rGO) was cycled under similar conditions (Supplementary Fig. S9). However, these papers were very brittle and required special handling during cell assembly. The first cycle discharge and charge capacities were observed to 943 and 347 mAhg⁻¹, respectively. Even though the first charge capacity was higher than other composite electrodes, the electrode started to show random spikes in the voltage profile with capacity drop after the second cycle itself. Therefore, rate capability tests were only performed on the best performing electrode specimen *i.e.*, 60MoS₂. As shown in Fig. 3d, the electrode stabilized to a charge capacity of 240 mAhg⁻¹ at a current density of 25 mA g⁻¹ (with respect to total weight of the electrode) after initial 5 cycles. The charge capacity remained stable (214 mAhg⁻¹, 90 % retention) even at current densities as high 100 mA g⁻¹. The electrode regained most of its charge capacity (230 mAhg⁻¹, 96% retention) when the current density was brought back to 25 mA g⁻¹ after 15 cycles. On further increasing the current density to 200 mA g⁻¹, 72% (173 mAhg⁻¹) of the initial stable capacity was retained. And again when the current density was brought back to initial 25 mA g⁻¹, the electrode recovered 87 % of its capacity and remained stable for another 5 cycles. It is remarkable that even at 200 mA g⁻¹, the electrode had a stable charge/discharge cycles with no abnormalities, which suggests the improved mechanical stability of this interleaved architecture. Summary of the electrochemical data is presented in Table S3.

Further, to check the integrity of the electrode specimen, the cells were disassembled and the electrode recovered for further characterization. Supplementary Fig. S10 shows the digital photographs (a-e), low resolution (f-j) and high-resolution (k-o) SEM images of the disassembled cells after 20 cycles. No evidence of surface cracks, volume change or physical imperfections could be observed in the SEM image, suggesting high mechanical/structural strength of the MoS₂/rGO composite paper. In all cases, the evidence of formation of a thin layer covering the electrode surface, possibly the SEI layer could be observed. The contamination in the specimen, indicated by the arrows, is from the residue of glass separator fibers. Also, these anodes may have been exposed to air during the transfer process resulting in oxidation of Na species, which appeared as bright spots

in the images (due to its non-conducting nature). Supplementary Fig. S11 shows the images obtained by EDX mapping of the electrode surface. Table S2 shows the at. wt % of various elements detected during the EDX mapping. A high percentage of sodium (19.46 at. %) was observed on the electrode surface, which is generally attributed to formation of SEI layer during the electrochemical cycling process. Even higher percentage of surface oxygen (41.46 at. %) was observed, which may have come from oxidation of intercalated sodium metal. Further analysis involved disassembling 60MoS₂ cell after 1st discharge cycle. TEM images in Fig. 4 (a) show degradation of MoS₂ sheets and possible amorphization (ring like SAED pattern).⁶⁷ Complementary results were observed in XRD and XPS analysis of the fully sodiated electrode as shown in Fig. 4 (b) and Supplementary Fig. S12, respectively. Broad Mo peak and Na-S peaks could be identified in both XRD (Mo at 29°, Na-S at 72° 2θ) and XPS (Mo at 231 eV, Na-S at 160.6 eV) spectrum. Also, the primary MoS₂ peak at 14° 2θ (002) appeared broadened, further indicating degradation of MoS₂ structure, most likely due to a conversion type reaction with Na-ions.⁶⁸⁻⁷⁰

Based on the voltage profiles, differential capacity plots, GITT cycling data and post cycling analysis, we predict the mechanism of Na-ion's reaction with MoS₂-graphene composite to be a combination of intercalation and conversion type reaction that is generally observed in Li/TMDC³⁴ and cathodes for Na-ion batteries.⁷¹⁻⁷² Supplementary Fig. S13 shows an idealized rGO/MoS₂ structure (in reality however the acid treated MoS₂ sheets are wrapped by much larger rGO sheets) to illustrate the predicted reaction mechanism in 2.0 to 0.1 V range. Step 1 is seen as a combination of Na intercalation reaction into the ordered MoS₂ (~0.9 V) and later into the disordered Na_xMoS₂ layers (~0.8 V). While step 2 represents the conversion reaction resulting in breakdown of MoS₂ into Mo and Na₂S, as can be seen in the TEM (Fig. 4a), XRD (Fig. 4b), and XPS data from the fully sodiated cell in Supplementary Fig. S12 (further confirmed by the lower voltage plateau at ~0.12 V, that was not observed in the discharge of rGO electrode, Supplementary Fig. S7a). A more detailed analysis may be obtained from *in-situ* synchrotron powder diffraction⁷⁴ and spectroscopy studies similar to as demonstrated by Grey's group on LIBs.^{75,76}

The tensile strength and strain to failure are important parameters for any flexible battery electrode. Therefore, the rGO, 40MoS₂ and 60MoS₂ papers were subjected to static uniaxial tensile testing in a custom built set-up (see methods and Fig. 5a). As can be seen, the specimen strip is secured on one end by a computer controlled movable stage, while the other end is fixed to a load cell, which in turn is fixed to an immovable stage. Engineering stress-strain plots derived from load-displacement data are shown in Fig. 5b. 40MoS₂ showed higher fracture strength and modulus (approx. 7.8 MPa and 424 MPa) than 60MoS₂ (approx. 2.1 MPa and 120 MPa) composite paper. On comparison, rGO had fracture strength and modulus of approx. 12 MPa and 885 MPa, respectively. The tensile strength of rGO paper is comparable to those reported by Nyugen's group involving *in-situ* reduced GO papers.⁷⁶ These values are however, much lower than GO papers but this is hardly surprising considering that our papers were annealed at high temperatures (500 °C for 2h and 900 °C for 5 min) and the mechanical strength of GO generally decreases with increasing annealing temperatures caused by release of oxygen groups that disturbs the structure of the paper resulting in a highly crumpled configuration.⁷⁷ The strain to failure was higher in case of 60MoS₂ specimen reaching values in excess of approx. 2 %. A total of five specimens were tested for 40MoS₂ and 60MoS₂ paper each that are shown in the photographic image in Fig. 5c and d, respectively. Data is summarized in Table 1. Fig. 5e and f are the corresponding SEM images of the fractured edge for 40MoS₂ and 60MoS₂, respectively. The edge was observed to be more regular and smooth for 60MoS₂ than for 40MoS₂. The variation in strain to failure for the composite specimen is attributed partially to the likely inhomogeneity in the specimens (large size of the paper and higher loading 4 mg.cm⁻²) and crumpled nature of the rGO layers. Subsequently, combined with observations in SEM images, 60MoS₂ had even larger variation in failure strain as the more slippery MoS₂ sheets can slide better than crumpled rGO sheets.

Conclusion

We have demonstrated synthesis of a composite layered paper consisting of acid exfoliated MoS₂ nanoflakes in an rGO matrix. Mechanical tests involving static

uniaxial tension reveal mechanical strength that was approx. 2 to 3 MPa and high failure strain (approx. 2 %) in these materials. Further, the composite paper was directly utilized as counter electrode in Na-ion battery half-cell and its performance was evaluated as a potential anode for use in a Na-ion battery full cell. These tests revealed high first cycle electrochemical capacity of 338 mAhg^{-1} with respect to total weight of the electrode with excellent cycleability of Na-ions. This study provides the first experimental evidence of reversible electrochemical storage of Na in layered self-standing MoS_2 composite electrode at room temperatures and is expected to open new avenues for use of large area free-standing binder-free flexible electrodes for rechargeable battery applications.

Methods, Materials and Instrumentation

ζ potential surface measurements were carried out on a ZetaPlus Zeta Potential Analyzer (Brookhaven's Inst. Corp.). The effect of ionic concentration on the potential measured is minimized by using a low concentration of basic (0.01 M NaOH) solution for controlling the pH. Scanning electron microscopy (SEM) of the synthesized material was carried out on a Carl Zeiss EVO MA10 system with incident voltage of 5 KV to 30 KV. TEM images were digitally acquired by use of a Phillips CM100 operated at 100 KV. Material characterization was made using X-ray diffractometer (XRD) operating at room temperature, with nickel-filtered $\text{CuK}\alpha$ radiation ($\lambda=1.5418 \text{ \AA}$). Thermogravimetric analysis (TGA) was performed using Shimadzu 50 TGA (limited to $800 \text{ }^\circ\text{C}$). Samples weighing, $\sim 2.5 \text{ mg}$, were heated in a platinum pan at a rate of $10 \text{ }^\circ\text{C}\cdot\text{min}^{-1}$ in air flowing at $20 \text{ mL}\cdot\text{min}^{-1}$. Raman spectra were measured using a LabRAM ARMIS Raman spectrometer using 633 nm laser excitation (laser power of 17 mW) as the light source. The surface chemical composition was studied by X-ray photoelectron spectroscopy (XPS, PHI Quantera SXM) using monochromatic Al $\text{K}\alpha$ X-radiation. Static uniaxial in-plane tensile tests were conducted in a simple test setup. The sample strip is secured on one end by a computer controlled movable stage (M-111.2DG from PI®), while the other end it is fixed to a 1N load cell (ULC-1N Interface®), which in turn is fixed to an immovable stage. All tensile tests were conducted in controlled strain rate mode with a strain rate of $0.2 \text{ \%}\cdot\text{min}^{-1}$. The samples were cut with a razor into rectangular strips of

approximately $5 \times 15 \text{ mm}^2$ for testing without further modification. Electrical conductivity measurements were carried out by use of a four-point probe setup and Keithley 2636A (Cleveland, OH) dual channel sourcemeter in the ohmic region. Electrochemical cycling of the assembled cells was carried out using multichannel Battery Test Equipment (Arbin-BT2000, Austin, TX) at atmospheric conditions.

Preparation graphene oxide

Sodium nitrate (99.2%), potassium permanganate (99.4%), sulfuric acid (96.4 %), hydrogen peroxide (31.3 % solution in water), hydrochloric acid (30 % solution in water), methanol (99.9 %) were purchased from Fisher Scientific. All materials were used as received without further purification. Modified Hummer's method was used to make graphene oxide.⁴⁹ Concentrated H_2SO_4 (130 mL) was added to a mixture of graphite flakes (3 g) and NaNO_3 (1.5 g). The mixture was cooled down using an ice bath. KMnO_4 was added slowly to this mixture. The mixture was stirred for 12 h at 50 °C. Then it was quenched with water (400 mL) with 30 % H_2O_2 (3 mL) while in an ice bath such that the temperature does not go beyond 20 °C. The remaining material was then washed in succession with 200 mL of water twice, 200 mL of 30 % HCl and 200 mL of ethanol. The material remaining after these extended washes is coagulated with 200 mL of ether and filtered through a paper filter. The filtrate is dried overnight to obtain dry graphene oxide (GO).

Preparation of exfoliated or acid treated MoS_2 flakes

MoS_2 powder (2 mg.mL^{-1} , 99 %, Sigma Aldrich) was sonicated for 30 min in concentrated chlorosulfonic acid (superacid, 99%, Sigma Aldrich), and the non-exfoliated sheets were allowed to settle. Please note that the superacid was very slowly added to the MoS_2 powder in an argon-filled glovebox (dew point $-50 \text{ }^\circ\text{C}$). The solution was then carefully quenched in 1.0 L of distilled water (done with extreme caution in a glovebox). Additional dilution with DI water was done to reduce the solution acidity. The solution was then dried in a conventional oven to obtain dry superacid treated MoS_2 ($\text{MoS}_2\text{-SA}$).

Preparation of reduced graphene oxide and MoS_2 composite paper

The composite papers were prepared in two sizes: 1.8" and 6.25" diameters. Small size papers were prepared to save material costs and time (since coin cells could only accommodate specimen approx. 1.4 cm in diameter). Large size paper was prepared only for 60MoS₂ electrode since it was the best performing specimen and most challenging to prepare considering the high percentage of MoS₂ in it.

Small size papers: 15 mg GO and varying wt. % of MoS₂ (prepared from the procedure state above) were mixed together in 1:1 (v/v) water and isopropanol solution. The mixture was then sonicated for 60 min (Branson Sonifier S-450A, 400 W). The composite suspension was then filtered by vacuum filtration process through a 47 mm diameter 10 μm pore sized filter membrane (HPLC grade, Millipore). MoS₂/GO composite paper thus obtained was dried in an oven at 70 °C overnight and subsequently reduced at 500 °C for 2h and 900 °C for 5 min in argon atmosphere. The samples were labeled as rGO, 20MoS₂, 40MoS₂ and 60MoS₂ for pristine rGO paper and rGO with 20, 40 and 60 % of MoS₂ in the total weight of the paper, respectively. The 60MoS₂-raw paper was synthesized with as-obtained MoS₂ and GO, following the process stated above. Later, the large-area paper with 60MoS₂ composition (approx. 6.25" diameter, cut into rectangular strip shown in Fig. 2b) was prepared following similar procedure by use of a Büchner funnel with a polypropylene filter paper (Celgard®).

Coin Cell/Battery assembly

For electrochemical testing, 2032 half coin cells were made by punching 14.3 mm diameter out of the composite paper for use as working electrode. 1M NaClO₄ (Alfa Aesar) in (1:1 v/v) dimethyl carbonate:ethylene carbonate (ionic conductivity 10.7 mS cm⁻¹) served as the electrolyte. A 25 μm thick (19 mm diameter) glass separator soaked in electrolyte was placed between the working electrode and pure Na metal (14.3 mm diameter, 75 μm thick) counter electrode. Washer, spring and a top casing were placed on top to complete the assembly before crimping. The assembled cells were tested using multichannel BT2000 Arbin test unit sweeping between 2.25 V to 10 mV v/s Na/Na⁺. C-rate performance of the best performing electrode material (60MoS₂) was tested in the voltage range from 2.25 V to 0.1 V

vs Na/Na⁺ using the following cycle schedule: Na⁺ was inserted at 100 mA g⁻¹ while the extraction was performed at current densities of 25, 50, 100, 25, 150, 200 and 25 mA g⁻¹ for 5 cycles consecutively.

Associated Content

Supporting information

TEM images, SAED pattern, SEM images, Elemental mapping data, X-ray photoelectron spectroscopy data, X-ray diffraction data, Raman spectroscopy data, GITT data for rGO and 60MoS₂ electrodes, Voltage profiles, post electrochemical analysis, summary of electrical conductivity data. This material is available free of charge *via* the Internet at <http://pubs.acs.org>.

Author information

Corresponding author

*E-mail: gurpreet@ksu.edu, Tel.: +1-785-532-7085, Fax: +1-785-532-7057

Present address: Department of Mechanical and Nuclear Engineering, Kansas State University, Manhattan, KS 66506, USA

Acknowledgements

L.D. would like to thank Erin Black for assistance with specimen preparation. We thank Professor Kevin Lease and Nassim Rahmani (K-State) for access to their lab for mechanical testing. Thanks are also due to Dr. Andras Kis (EPFL) and Dr. Scott Bunch (BU) for visit to K-State and useful discussions related to layered materials. G.S. thanks Michele Anderson (ONR) for encouragement to pursue this research.

Author contribution

L.D. performed most experiments including composite paper preparation, annealing, electrochemical and mechanical testing. R.B. prepared electrolyte solution and performed Zeta potential experiments. G.S. conceived the idea, designed the experiments and wrote the manuscript with inputs from L.D. All authors discussed the results and commented or revised the manuscript.

References

1. Armand, M.; Tarascon, J. M. Building Better Batteries. *Nature*, **2008**, *451*, 652-657.
2. Manthiram, A.; Fu, Y.; Su, Y. S. In Charge of the World: Electrochemical Energy Storage. *J. Phys. Chem. Lett.* **2013**, *4*, 1295-1297
3. Saravanan, K.; Mason, C. W.; Rudola, A.; Wong, K. H.; Balaya, P. The First Report on Excellent Cycling Stability and Superior Rate Capability of $\text{Na}_3\text{V}_2(\text{PO}_4)_3$ for Sodium Ion Batteries. *Adv. Energy Mater.* **2013**, *3*, 444-450.
4. Tarascon, J. M. Is Lithium The New Gold? *Nat. Chem.*, **2010**, *2*, 510.
5. Ellis, B. L.; Makahnouk, W. R. M.; Makimura, Y.; Toghill, K.; Nazar, L. F. A Multifunctional 3.5 V Iron-Based Phosphate Cathode For Rechargeable Batteries *Nat. Mater.*, **2007**, *6*, 749-753.
6. Kim, D.; Kang, S. H.; Slater, M.; Rood, S.; Vaughey, J. T.; Karan, N.; Balasubramanian, M.; Johnson, C. S. Enabling Sodium Batteries Using Lithium-Substituted Sodium Layered Transition Metal Oxide Cathodes. *Adv. Energy Mater.* **2011**, *1*, 333-336.
7. Cao, Y.; Xiao, L.; Wang, W.; Choi, D.; Nie, Z.; Yu, J.; Saraf, L. V.; Yang, Z.; Liu, J. Reversible Sodium Ion Insertion in Single Crystalline Manganese Oxide Nanowires with Long Cycle Life. *Adv. Mater.* **2011**, *23*, 3155-3160.
8. Ellis, B. L.; Nazar, L. F., Sodium and Sodium-Ion Energy Storage Batteries. *Curr. Opin. Solid State Mater. Sci.* **2012**, *16*, 168-177.
9. Chevrier, V. L.; Ceder, G. Challenges for Na-ion Negative Electrodes. *J. Electrochem. Soc.* **2011**, *158*, A1011-A1014.
10. Lin, Y. M.; Abel, P. R.; Gupta, A.; Goodenough, J. B.; Heller, A.; Mullins, C. B. Sn-Cu Nanocomposite Anodes for Rechargeable Sodium-Ion Batteries. *ACS Appl. Mater. Interfaces* **2013**, *5*, 8273-8277.
11. Darwiche, A.; Marino, C.; Sougrati, M. T.; Fraise, B.; Stievano, L.; Monconduit, L. Better Cycling Performances of Bulk Sb in Na-Ion Batteries Compared to Li-Ion Systems: An Unexpected Electrochemical Mechanism. *J. Am. Chem. Soc.* **2012**, *134*, 20805-20811.

12. Xiao, L.; Cao, Y.; Xiao, J.; Wang, W.; Kovarik, L.; Nie, Z.; Liu, J. High capacity, Reversible Alloying Reactions in SnSb/C Nanocomposites for Na-Ion Battery Applications. *Chem. Commun.* **2012**, *48*, 3321-3323.
13. Qian, J.; Chen, Y.; Wu, L.; Cao, Y.; Ai, X.; Yang, H. High Capacity Na-Storage and Superior Cyclability of Nanocomposite Sb/C Anode for Na-Ion Batteries. *Chem. Commun.* **2012**, *48*, 7070-7072.
14. Qian, J.; Wu, X.; Cao, Y.; Ai, X.; Yang, H. High Capacity and Rate Capability of Amorphous Phosphorus for Sodium Ion Batteries. *Angew. Chem., Int. Ed.* **2013**, *52*, 4633-4636.
15. Kim, Y.; Park, Y.; Choi, A.; Choi, N.S.; Kim, J.; Lee, J.; Ryu, J. H.; Oh, S. M.; Lee, K. T. An Amorphous Red Phosphorus/Carbon Composite as a Promising Anode Material for Sodium Ion Batteries. *Adv. Mater.* **2013**, *25*, 3045-3049.
16. Xiong, H.; Slater, M. D.; Balasubramanian, M.; Johnson, C. S.; Rajh, T. Amorphous TiO₂ Nanotube Anode for Rechargeable Sodium Ion Batteries. *J. Phys. Chem. Lett.* **2011**, *2*, 2560-2565.
17. Zhu, H.; Jia, Z.; Chen, Y.; Weadock, N.; Wan, J.; Vaaland, O.; Han, X.; Li, T.; Hu, L. Tin Anode for Sodium-Ion Batteries Using Natural Wood Fiber as a Mechanical Buffer and Electrolyte Reservoir. *Nano Lett.* **2013**, *13*, 3093-3100.
18. Zhu, Y.; Han, X.; Xu, Y.; Liu, Y.; Zheng, S.; Xu, K.; Hu, L.; Wang, C. Electrospun Sb/C Fibers for a Stable and Fast Sodium-Ion Battery Anode. *ACS Nano* **2013**, *7*, 6378-6386.
19. Stevens, D. A.; Dahn, J. R. High Capacity Anode Materials for Rechargeable Sodium-Ion Batteries. *J. Electrochem. Soc.* **2000**, *147*, 1271-1273.
20. Alcántara, R.; Jiménez-Mateos, J. M.; Lavela, P.; Tirado, J. L. Carbon Black: A Promising Electrode Material for Sodium-Ion Batteries. *Electrochem. Commun.* **2001**, *3*, 639-642.
21. Alcántara, R.; Jiménez Mateos, J. M.; Tirado, J. L. Negative Electrodes for Lithium- and Sodium-Ion Batteries Obtained by Heat-Treatment of Petroleum Cokes below 1000°C. *J. Electrochem. Soc.* **2002**, *149*, A201-A205.
22. Komaba, S.; Murata, W.; Ishikawa, T.; Yabuuchi, N.; Ozeki, T.; Nakayama, T.; Ogata, A.; Gotoh, K.; Fujiwara, K. Electrochemical Na Insertion and Solid

- Electrolyte Interphase for Hard-Carbon Electrodes and Application to Na-Ion Batteries. *Adv. Funct. Mater.* **2011**, *21*, 3859-3867.
23. Cao, Y.; Xiao, L.; Sushko, M. L.; Wang, W.; Schwenzler, B.; Xiao, J.; Nie, Z.; Saraf, L. V.; Yang, Z.; Liu, J. Sodium Ion Insertion in Hollow Carbon Nanowires for Battery Applications. *Nano Lett.* **2012**, *12*, 3783-3787.
24. Palacin, M. R. Recent Advances in Rechargeable Battery Materials: A Chemist's Perspective. *Chem. Soc. Rev.* **2009**, *38*, 2565-2575.
25. Ponrouch, A.; Goñi, A. R.; Palacín, M. R. High Capacity Hard Carbon Anodes for Sodium Ion Batteries in Additive Free Electrolyte. *Electrochem. Commun.* **2013**, *27*, 85-88.
26. Liu, H.; Su, D.; Zhou, R.; Sun, B.; Wang, G.; Qiao, S. Z. Highly Ordered Mesoporous MoS₂ with Expanded Spacing of the (002) Crystal Plane for Ultrafast Lithium Ion Storage. *Adv. Energy Mater.* **2012**, *2*, 970-975.
27. Tepavcevic, S.; Xiong, H.; Stamenkovic, V. R.; Zuo, X.; Balasubramanian, M.; Prakapenka, V. B.; Johnson, C. S.; Rajh, T. Nanostructured Bilayered Vanadium Oxide Electrodes for Rechargeable Sodium-Ion Batteries. *ACS Nano* **2011**, *6*, 530-538.
28. Hu, Y.; Li, X.; Lushington, A.; Cai, M.; Geng, D.; Banis, M. N.; Li, R.; Sun, X. Fabrication of MoS₂-Graphene Nanocomposites by Layer-by-Layer Manipulation for High-Performance Lithium Ion Battery Anodes. *ECS J. Solid State Sci. Technol.* **2013**, *2*, M3034-M3039.
29. Xiao, J.; Wang, X.; Yang, X. Q.; Xun, S.; Liu, G.; Koech, P. K.; Liu, J.; Lemmon, J. P. Electrochemically Induced High Capacity Displacement Reaction of PEO/MoS₂/Graphene Nanocomposites with Lithium. *Adv. Funct. Mater.* **2011**, *21*, 2840-2846.
30. Zhou, X.; Wan, L. J.; Guo, Y. G. Facile Synthesis of MoS₂@CMK-3 Nanocomposite As An Improved Anode Material for Lithium-Ion Batteries. *Nanoscale* **2012**, *4*, 5868-5871.
31. Hwang, H.; Kim, H.; Cho, J. MoS₂ Nanoplates Consisting of Disordered Graphene-like Layers for High Rate Lithium Battery Anode Materials. *Nano Lett.* **2011**, *11*, 4826-4830.

32. Chang, K.; Chen, W. I-Cysteine-Assisted Synthesis of Layered MoS₂/Graphene Composites with Excellent Electrochemical Performances for Lithium Ion Batteries. *ACS Nano* **2011**, *5*, 4720-4728.
33. Zhao, X.; Hayner, C. M.; Kung, M. C.; Kung, H. H. Flexible Holey Graphene Paper Electrodes with Enhanced Rate Capability for Energy Storage Applications. *ACS Nano* **2011**, *5*, 8739-8749.
34. Cabana, J.; Monconduit, L.; Larcher, D.; Rosa Palacin, M. Beyond Intercalation-Based Li-Ion Batteries: The State of the Art and Challenges of Electrode Materials Reacting Through Conversion Reactions. *Adv. Mater.* **2010**, *22*, E170-E192.
35. Ji, H.; Zhang, L.; Pettes, M. T.; Li, H.; Chen, S.; Shi, L.; Piner, R.; Ruoff, R. S. Ultrathin Graphite Foam: A Three-Dimensional Conductive Network for Battery Electrodes. *Nano Lett.* **2012**, *12*, 2446-2451.
36. Hwang, H.; Kim, H.; Cho, J. MoS₂ Nanoplates Consisting of Disordered Graphene-like Layers for High Rate Lithium Battery Anode Materials. *Nano Lett.* **2011**, *11*, 4826-4830.
37. Chhowalla, M. ; Shin, H. S.; Eda, G.; Li, L. J.; Loh, K. P.; Zhang, H. The Chemistry of Two-Dimensional Layered Transition Metal Dichalcogenide Nanosheets. *Nat. Chem.* **2013**, *5*, 263-275.
38. Ge, P.; Foulletier, M. Electrochemical Intercalation of Sodium in Graphite. *Solid State Ionics* **1988**, *28-30, Part 2*, 1172-1175.
39. Stevens, D. A.; Dahn, J. R. The Mechanisms of Lithium and Sodium Insertion in Carbon Materials. *J. Electrochem. Soc.* **2001**, *148*, A803-A811.
40. Asher, R. C. A Lamellar Compound of Sodium and Graphite. *J. Inorg. Nucl. Chem.* **1959**, *10*, 238-249.
41. Hu, L.; Choi, J. W.; Yang, Y.; Jeong, S.; La Mantia, F.; Cui, L.F.; and Cui, Y. Highly Conductive Paper for Energy-Storage Devices. *Proc. Natl. Acad. Sci. U. S. A.*, **2009**, *106*, 21490-21494.
42. Cui, L. F.; Hu, L.; Choi, J. W.; and Cui, Y. Light-Weight Free-Standing Carbon Nanotube-Silicon Films for Anodes of Lithium Ion Batteries. *ACS Nano*, **2010**, *4*, 3671-3678.

43. Wang, D.; Kou, R.; Choi, D.; Yang, Z.; Nie, Z.; Li, J.; Saraf, L. V.; Hu, D.; Zhang, J.; Graff, G. L. *et al.* Ternary Self-Assembly of Ordered Metal Oxide–Graphene Nanocomposites for Electrochemical Energy Storage. *ACS Nano* **2010**, *4*, 1587-1595.
44. Li, N.; Chen, Z.; Ren, W.; Li, F.; Cheng, H. M. Flexible Graphene-Based Lithium Ion Batteries With Ultrafast Charge and Discharge Rates. *Proc. Natl. Acad. Sci. U. S. A.* **2012**, *109*, 17360-17365.
45. Zhao, X.; Hayner, C. M.; Kung, M. C.; Kung, H. H. In-Plane Vacancy-Enabled High-Power Si–Graphene Composite Electrode for Lithium-Ion Batteries. *Adv. Energy Mater.* **2011**, *1*, 1079-1084.
46. Abouimrane, A.; Compton, O. C.; Amine, K.; Nguyen, S. T. Non-Annealed Graphene Paper as a Binder-Free Anode for Lithium-Ion Batteries. *J. Phys. Chem. C* **2010**, *114*, 12800-12804.
47. Koo, M.; Park, K. I.; Lee, S. H.; Suh, M.; Jeon, D. Y.; Choi, J. W.; Kang, K.; Lee, K. J. Bendable Inorganic Thin-Film Battery for Fully Flexible Electronic Systems. *Nano Lett.* **2012**, *12*, 4810-4816.
48. Magasinski, A.; Dixon, P.; Hertzberg, B.; Kvit, A.; Ayala, J.; Yushin, G. High-Performance Lithium-Ion Anodes Using a Hierarchical Bottom-Up Approach. *Nat. Mater.* **2010**, *9*, 353-358.
49. Hummers, W. S.; Offeman, R. E. Preparation of Graphitic Oxide. *J. Am. Chem. Soc.* **1958**, *80*, 1339-1339.
50. Bhandavat, R.; David, L.; Singh, G. Synthesis of Surface-Functionalized WS₂ Nanosheets and Performance as Li-Ion Battery Anodes. *J. Phys. Chem. Lett.* **2012**, *3*, 1523-1530.
51. Lotya, M.; Hernandez, Y.; King, P. J.; Smith, R. J.; Nicolosi, V.; Karlsson, L. S.; Blighe, F. M.; De, S.; Wang, Z.; McGovern, I. T. *et al.* Liquid Phase Production of Graphene by Exfoliation of Graphite in Surfactant/Water Solutions. *J. Am. Chem. Soc.* **2009**, *131*, 3611-3620.
52. Coleman, J. N.; Lotya, M.; O'Neill, A.; Bergin, S. D.; King, P. J.; Khan, U.; Young, K.; Gaucher, A.; De, S.; Smith, R. J. *et al.* Two-Dimensional Nanosheets Produced by Liquid Exfoliation of Layered Materials. *Science* **2011**, *331*, 568-571.

53. Bertrand, P. A. Surface-Phonon Dispersion of MoS₂. *Phys. Rev. B* **1991**, *44*, 5745-5749.
54. Lee, C.; Yan, H.; Brus, L. E.; Heinz, T. F.; Hone, J.; Ryu, S. Anomalous Lattice Vibrations of Single- and Few-Layer MoS₂. *ACS Nano* **2010**, *4*, 2695-2700.
55. Chen, J. M.; Wang, C. S. Second order Raman spectrum of MoS₂. *Solid State Commun.* **1974**, *14*, 857-860.
56. Windom, B.; Sawyer, W. G.; Hahn, D. A Raman Spectroscopic Study of MoS₂ and MoO₃: Applications to Tribological Systems. *Tribol. Lett.* **2011**, *42*, 301-310.
57. Stacy, A. M.; Hodul, D. T. Raman Spectra of IVB and VIB Transition Metal Disulfides Using Laser Energies Near the Absorption Edges. *J. Phys. Chem. Solids* **1985**, *46*, 405-409.
58. Frey, G. L.; Tenne, R.; Matthews, M. J.; Dresselhaus, M. S.; Dresselhaus, G. Raman and Resonance Raman Investigation of MoS₂ Nanoparticles. *Phys. Rev. B* **1999**, *60*, 2883-2892.
59. Jiménez Sandoval, S.; Yang, D.; Frindt, R. F.; Irwin, J. C. Raman Study and Lattice Dynamics of Single Molecular Layers of MoS₂. *Phys. Rev. B* **1991**, *44*, 3955-3962.
60. Frey, G. L.; Reynolds, K. J.; Friend, R. H.; Cohen, H.; Feldman, Y. Solution-Processed Anodes from Layer-Structure Materials for High-Efficiency Polymer Light-Emitting Diodes. *J. Am. Chem. Soc.* **2003**, *125*, 5998-6007.
61. Du, G.; Guo, Z.; Wang, S.; Zeng, R.; Chen, Z.; Liu, H. Superior Stability and High Capacity of Restacked Molybdenum Disulfide as Anode Material for Lithium Ion Batteries. *Chem. Commun.* **2010**, *46*, 1106–1108.
62. Visic, B.; Dominko, R.; Gunde, M. K.; Hauptman, N.; Skapin, S. D.; Remskar, M. Optical Properties of Exfoliated MoS₂ Coaxial Nanotubes - Analogues of Graphene. *Nanoscale Res. Lett.* **2011**, *6*, 1-6.
63. Putz, K. W.; Compton, O. C.; Palmeri, M. J.; Nguyen, S. T.; Brinson, L. C. High-Nanofiller-Content Graphene Oxide-Polymer Nanocomposites *via* Vacuum-Assisted Self-Assembly. *Adv. Funct. Materials* **2010**, *20*, 3322-3329.
64. Cunningham, G.; Lotya, M.; McEvoy, N.; Duesberg, G. S.; van der Schoot, P.; Coleman, J. N. Percolation Scaling in Composites of Exfoliated MoS₂ Filled With Nanotubes and Graphene. *Nanoscale* **2012**, *4*, 6260-6264.

65. Stauffer, D and Aharony, A. Introduction to Percolation Theory, Taylor & Francis, London, 1985.
66. Wang, C.; Kakwana, I.; Appleby, A. J.; Little, F. E. *In Situ* Investigation of Electrochemical Lithium Intercalation Into Graphite Powder. *J. Electroanal. Chem.* **2000**, *489*, 55–67.
67. Firmiano, E. G. S.; Cordeiro, M. A. L.; Rabelo, A. C.; Dalmaschio, C. J.; Pinheiro, A. N.; Pereira, E. C.; Leite, E. R. Graphene Oxide as a Highly Selective Substrate to Synthesize a Layered MoS₂ Hybrid Electrocatalyst. *Chem. Commun.* **2012**, *48*, 7687-7689.
68. Hariharan, S.; Saravanan, K.; Balaya, P. α-MoO₃: A High Performance Anode Material for Sodium-Ion Batteries. *Electrochem. Commun.* **2013**, *31*, 5-9.
69. Das, S. K.; Mallavajula, R.; Jayaprakash, N.; Archer, L. A. Self-Assembled MoS₂-Carbon Nanostructures: Influence of Nanostructuring and Carbon on Lithium Battery Performance. *J. of Mater. Chem.* **2012**, *22*, 12988-12992.
70. Yang, L.; Yu, H.; Xu, L.; Ma, Q.; Qian, Y. Sulfur-Assisted Synthesis of Nitride Nanocrystals. *Dalton Trans.* **2010**, *39*, 2855-2860.
71. Kim, J. S.; Ahn, H. J.; Ryu, H. S.; Kim, D. J.; Cho, G. B.; Kim, K. W.; Nam, T. H.; Ahn, J. H. The Discharge Properties of Na/Ni₃S₂ Cell at Ambient Temperature. *J. Power Sources* **2008**, *178*, 852–856.
72. Park, J.; Kim, J.S.; Park, J.W.; Nama, T.H.; Kim, K.W.; Ahn, J.H.; Wang, G.; Ahn, H.J. Discharge Mechanism of MoS₂ for Sodium Ion Battery: Electrochemical Measurements and Characterization. *Electrochim. Acta* **2013**, *92*, 427– 432.
73. Misra, S.; Liu, N.; Nelson, J.; Hong, S. S.; Cui, Y.; Toney, M. F. *In Situ* X-ray Diffraction Studies of (De)lithiation Mechanism in Silicon Nanowire Anodes. *ACS Nano* **2012**, *6*, 5465-5473.
74. Bhattacharyya, R.; Key, B.; Chen, H.; Best, A.S.; Hollenkamp, A.F.; Grey, C.P. *In situ* NMR Observation of the Formation of Metallic Lithium Microstructures in Lithium Batteries. *Nat. Mater.* **2010**, *9*, 504-510.
75. Yamakawa, N.; Jiang, M.; Key, B.; Grey, C. P. A Study of the Lithium Conversion Mechanism of Iron Fluoride in a Li Ion Battery, by Using Solid State NMR, XRD and PDF Analysis Studies. *J. Am. Chem. Soc.* **2009**, *131*, 10525-10536.

76. Compton, O. C.; Dikin, D. A.; Putz, K. W.; Brinson, L. C.; Nguyen, S. T. Electrically Conductive "Alkylated" Graphene Paper *Via* Chemical Reduction of Amine-Functionalized Graphene Oxide Paper. *Adv. Mater.* **2010**, *22*, 892– 896.
77. Compton, O. C.; Nguyen, S. T. Graphene Oxide, Highly Reduced Graphene Oxide, and Graphene: Versatile Building Blocks for Carbon-Based Materials *Small* **2010**, *6*, 711– 723.

LIST OF FIGURES

FIGURE 1. (a) Photographic image showing acid treated MoS₂ immediately after it was quenched in 1 L of DI water at a concentration approx. 2 mg.mL⁻¹. SEM images showing the structure and size distribution of MoS₂ (b) before and (c) after superacid treatment. The particle size varied between (20 to 40) μm and approx. (1 to 20) μm for raw and acid treated MoS₂, respectively. The scale bar in the inset is 2 μm. (d-e) High-resolution TEM image of superacid treated MoS₂ (MoS₂-SA) sheets. (f) SAED pattern corresponding to TEM image in (e). (g) Graph showing calculated total interaction potential energy (V_T), repulsion (V_{DLVO}), and attraction energy (V_{vdw}) (per unit area) with increasing MoS₂ sheet separation distance (log scale) . Inset: Experimentally measured zeta potential, showing better dispersion stability at higher pH values. (h) Raman spectra of MoS₂ before and after acid treatment. The similarity in the relative intensity and position of the E_{2g}¹ and A_{1g} peaks suggests that the structure was largely undistorted MoS₂. (i) The change in intensity and FWHM of MoS₂ peak at 14° 2θ in the XRD spectra suggests increase in MoS₂ interlayer distance after the acid treatment (JCPDS #37-1492).

FIGURE 2. (a) Schematic representation showing synthesis of rGO/MoS₂ composite paper. (b) Digital picture showing large area composite paper prepared through vacuum filtration. (c) SEM top-view image of 60MoS₂ paper, insert shows the EDX spectra of spots in the SEM image indicating the material to be rGO (square) and MoS₂ (circle). The scale is 10 μm. (d) Corresponding SEM cross-sectional images shows the morphology of the paper. Average thickness of this paper was observed to be ~20 μm. (e) TEM image and SAED pattern of 60MoS₂. The MoS₂ sheets are

observed to be wrapped by much larger graphene sheets. In SAED pattern (insert), multiple spot pattern is observed one of which is due to the polycrystallinity of restacked rGO sheets while second set of spot pattern is assigned to MoS₂ sheets. The scale is 100 nm. (f) Thermogravimetric analysis data for MoS₂-SA, MoS₂-rGO composite paper and rGO paper. (g) Graph of electrical conductivity vs MoS₂ loading in the composite paper.

FIGURE 3. (a) Voltage profile of 60MoS₂ free-standing electrode along with its corresponding (b) differential capacity curves for the first two cycles. (c) Sodium charge capacity of various electrodes at a constant current density of 25 mA g⁻¹. (d) Sodium charge capacity and corresponding columbic efficiency of 60MoS₂ electrode cycled at varying current densities.

FIGURE 4. (a) TEM images and corresponding SAED patterns of 60MoS₂ electrode before and after 1st discharge cycle (0.01 V). The ring like SAED pattern suggests formation of nanocrystallites or amorphization of MoS₂ in the sodiated (discharged) electrode^{67,68}. (b) XRD pattern of 60MoS₂ electrode before and after 1st discharge cycle (0.01 V). Broadened MoS₂ (JCPDS #37-1492), rGO (JCPDS #01-0646), Mo (JCPDS #01-1207) and Na₂S (JCPDS #65-0525) peaks were observed in the sodiated electrode⁶⁸⁻⁷⁰.

FIGURE 5. (a) Tensile test setup (1: load cell, fixed, 2: clamps, top clamp not shown, 3: computer controlled moveable translation stage) with sample after fracture from loading (insert shows zoomed-in view of two such specimens). (b) Engineering stress-strain plot for rGO, 40MoS₂ and 60MoS₂ freestanding papers. Photographic image of (c) 40MoS₂ and (d) 60MoS₂ paper tested in this study. (e, and f) are the corresponding SEM cross-sectional images showing the fractured surface. The scale bar is 20 μm.

LIST OF TABLES

TABLE 1. Summary of tensile test data for rGO, 40MoS₂ and 60MoS₂ free-standing composite papers.

FIGURE 1

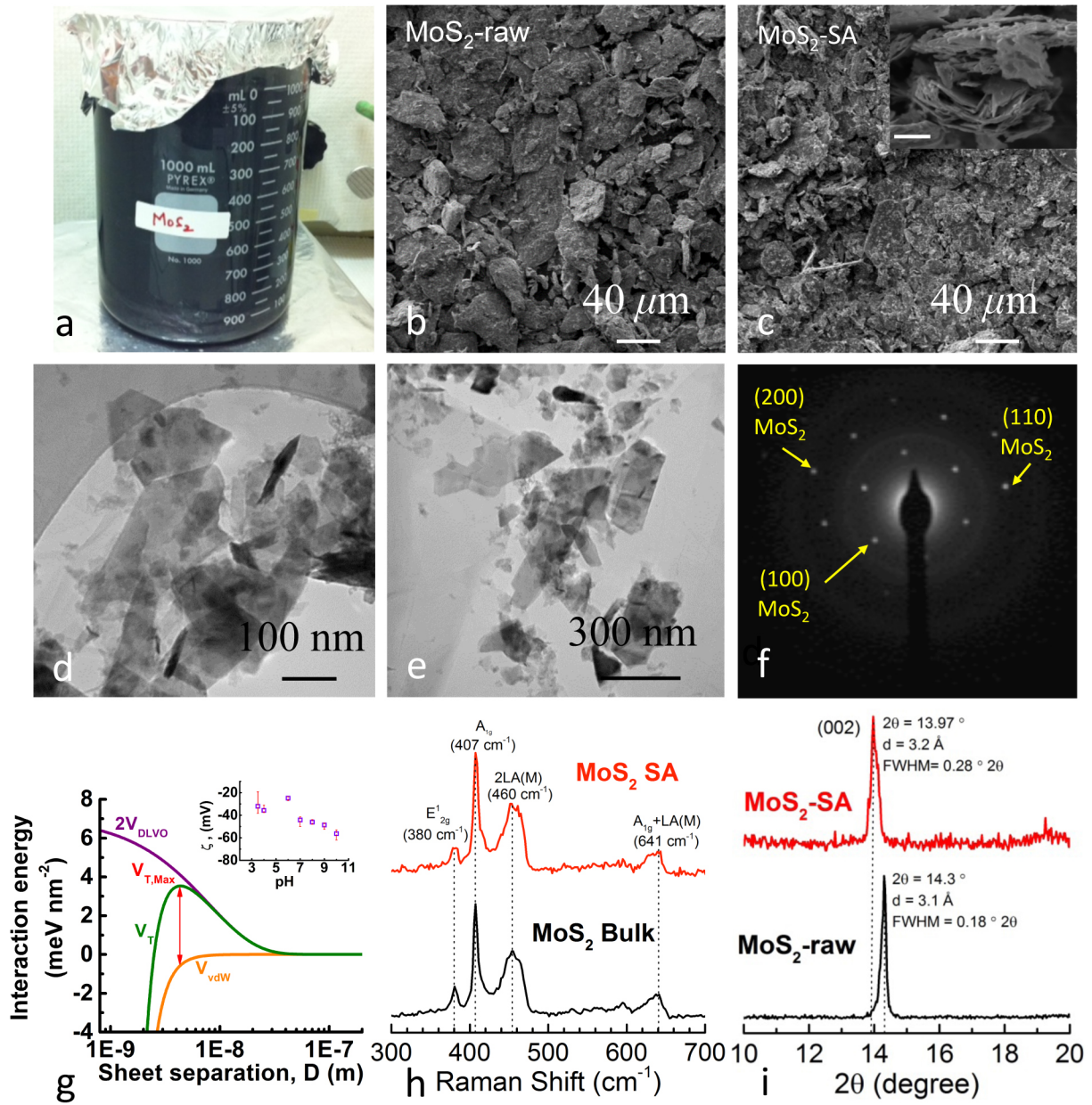


FIGURE 2

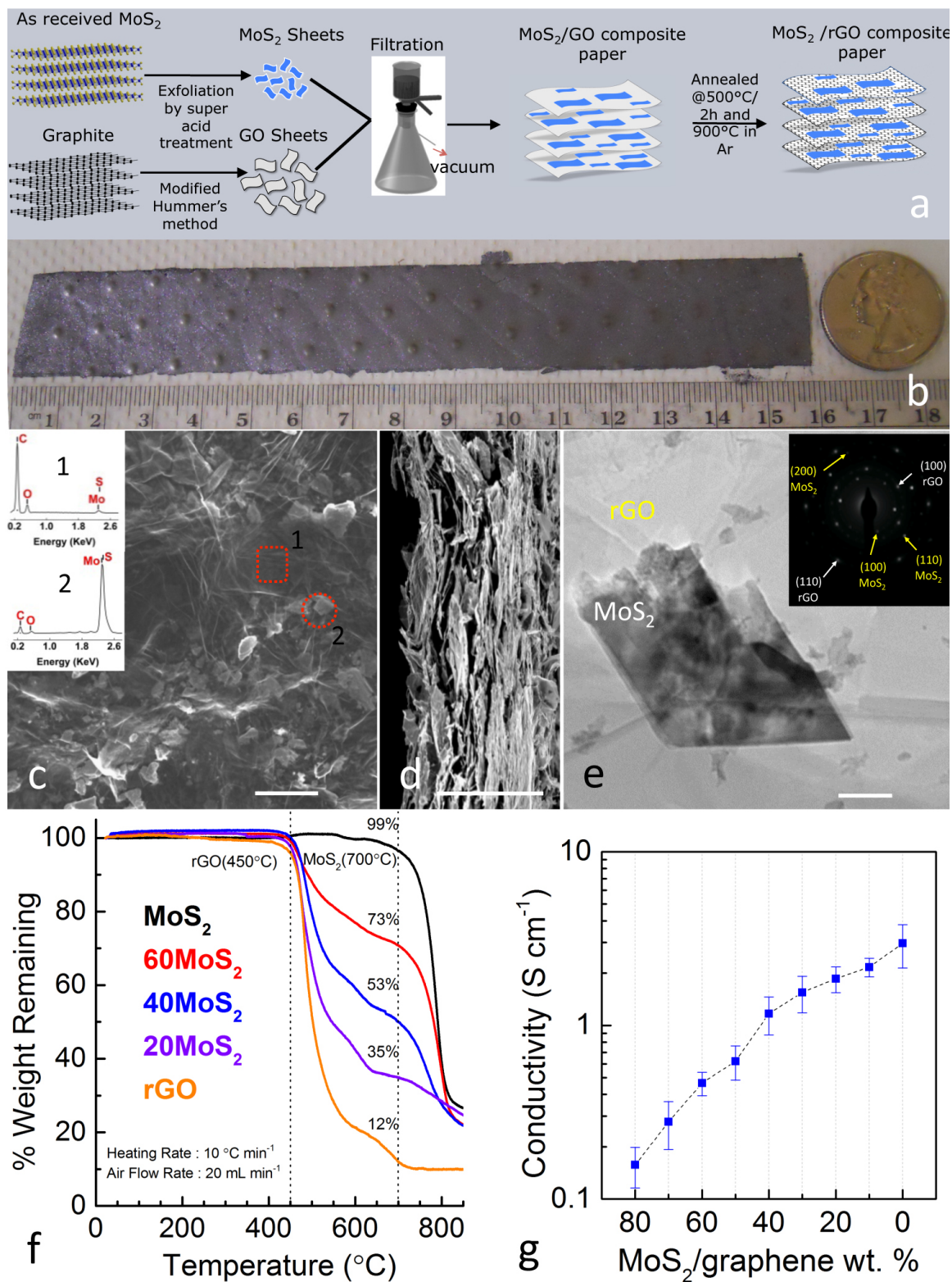


FIGURE 3

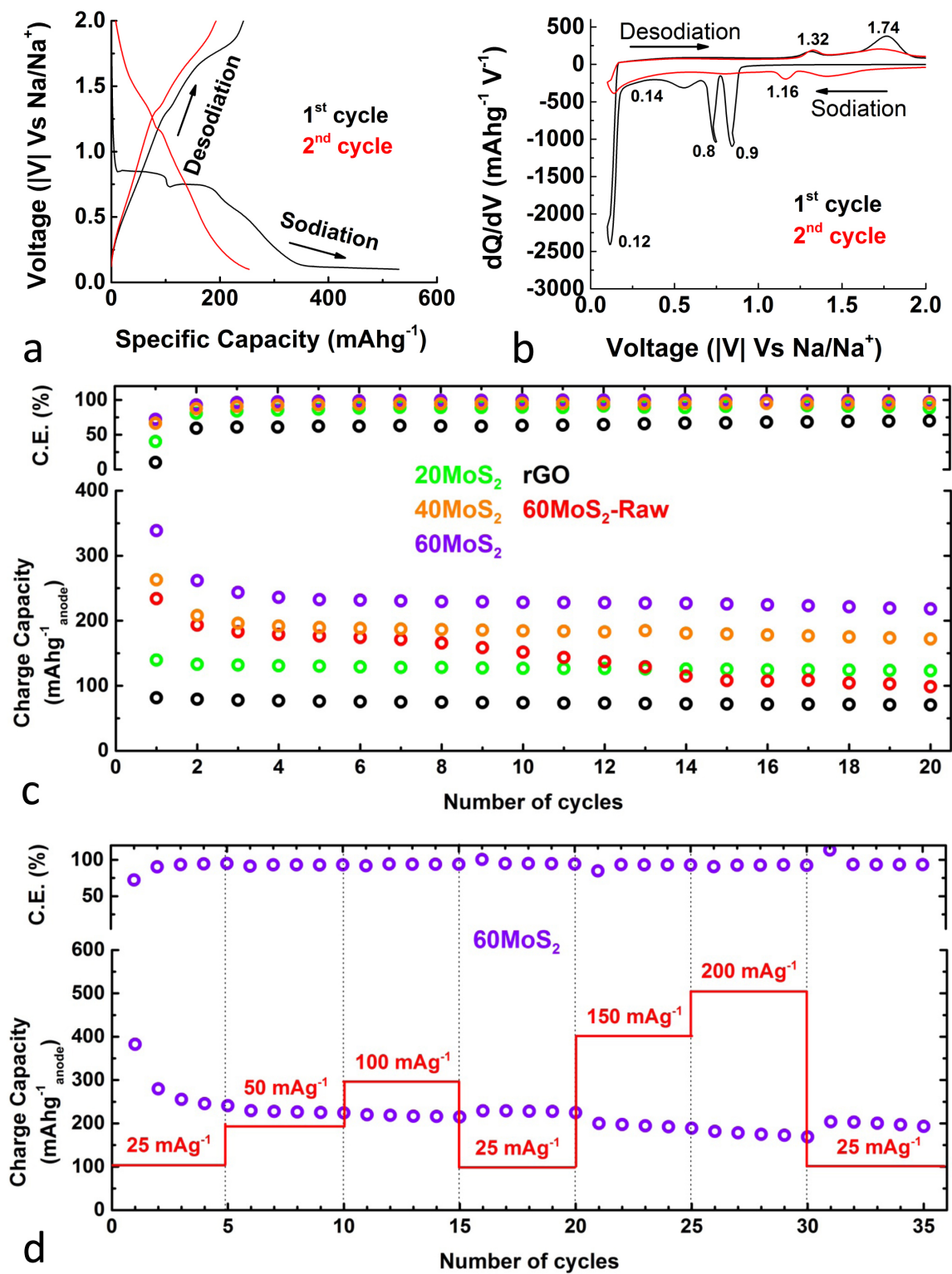


FIGURE 4

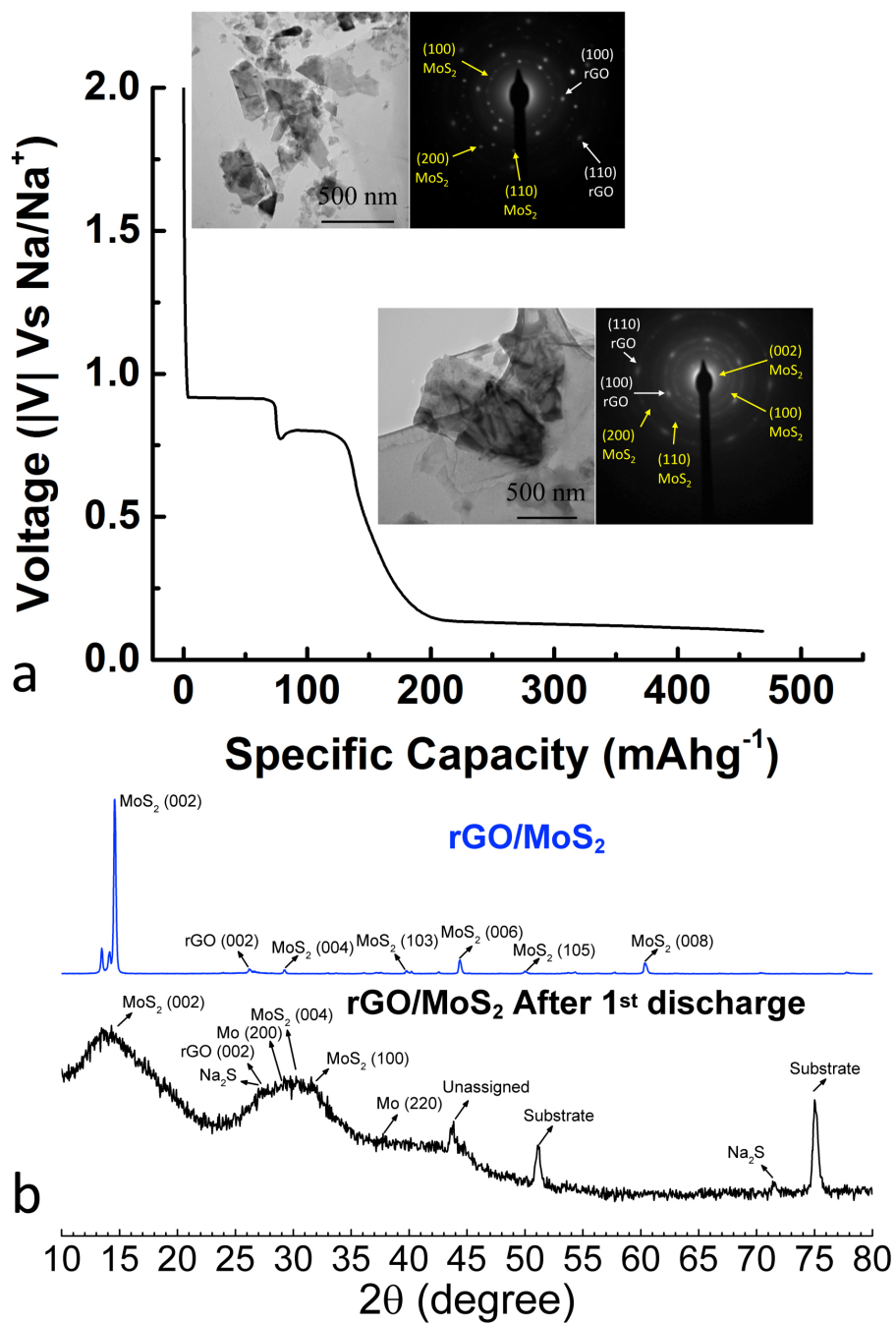


FIGURE 5

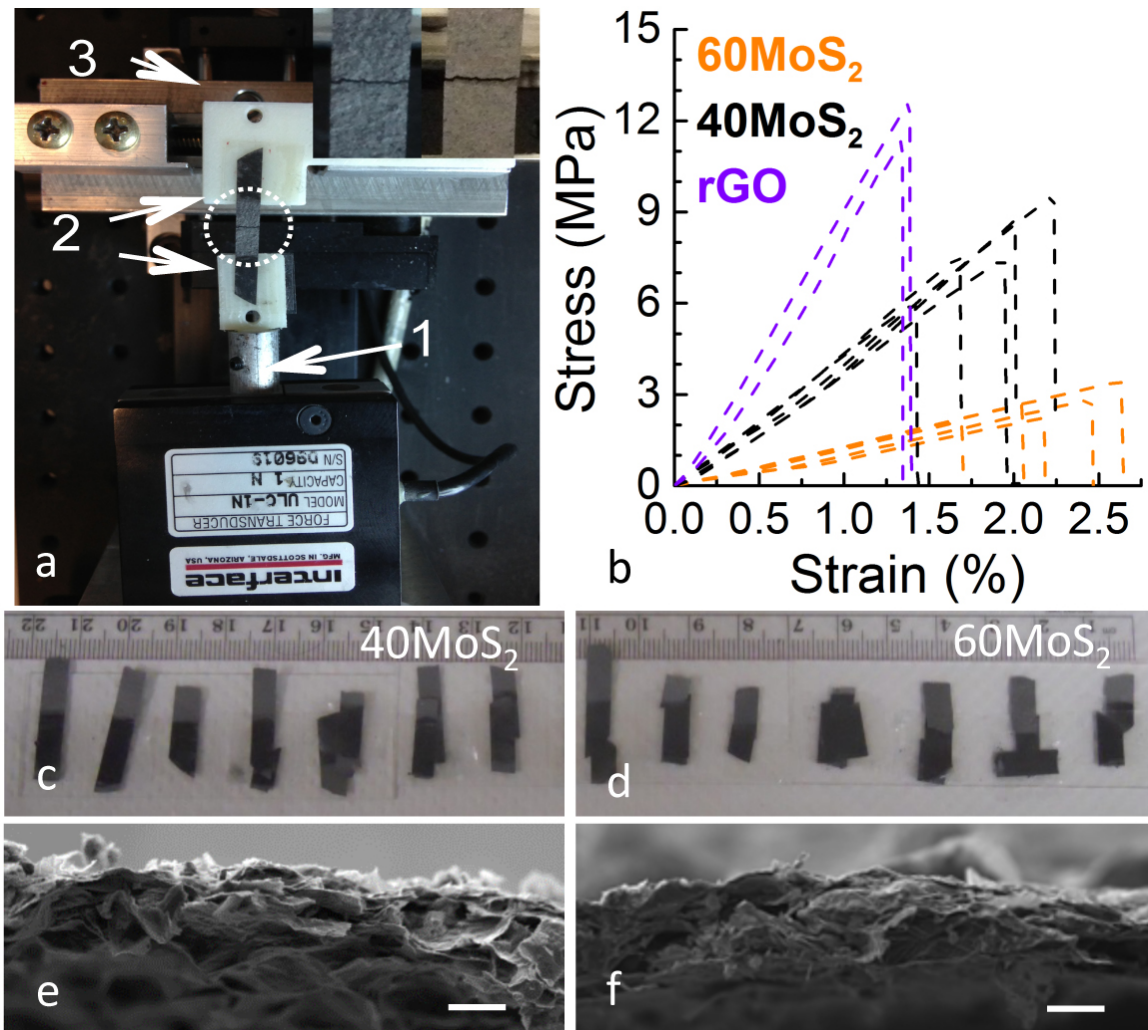


TABLE 1

Specimen	Modulus (MPa)	Tensile Strength (MPa)	Failure Strain (%)
rGO	897.86±18.86	12.57±0.13	1.4±0.014
	874.62±18.37	11.37±0.12	1.3±0.014
40MoS ₂	427.03±8.97	9.48±0.1	2.22±0.023
	434.5±9.12	8.69±0.09	2±0.021
	386.01±8.11	7.45±0.08	1.93±0.02
	450±9.45	7.56±0.08	1.68±0.017
	424.8±8.92	6.06±0.06	1.43±0.015
60MoS ₂	130.8±2.75	3.44±0.04	2.63±0.028
	115.92±2.43	2.84±0.03	2.45±0.026
	102.76±2.16	2.23±0.02	2.17±0.023
	131.22±2.76	2.69±0.03	2.05±0.021
	125.85±2.64	2.13±0.02	1.69±0.018

TOC Graphic

